ACS APPLIED MATERIALS & INTERFACES

Research Article

www.acsami.org

High-Efficiency Small-Molecule-Based Organic Light Emitting Devices with Solution Processes and Oxadiazole-Based Electron Transport Materials

Yung-Ting Chang,[†,‡,∥] Jan-Kai Chang,[‡,∥] Yi-Ting Lee,[†] Po-Sheng Wang,[‡] Jhao-Lin Wu,[†] Che-Chang Hsu,[‡] I-Wen Wu,[‡] Wei-Hsuan Tseng,[‡] Tun-Wen Pi,[§] Chin-Ti Chen,*[,†] and Chih-I Wu*[,‡]

[†]Institute of Chemistry, Academia Sinica, Taipei, Taiwan 11529, R. O. C.

[‡]Graduate Institute of Photonics and Optoelectronics and Department of Electrical Engineering, National Taiwan University, Taipei, Taiwan 10617, R. O. C.

[§]National Synchrotron Radiation Research Center, Hsinchu, Taiwan 30077, R. O. C.

Supporting Information

ABSTRACT: We demonstrate high-efficiency small-molecule-based white phosphorescent organic light emitting diodes (PHOLEDs) by single-active-layer solution-based processes with the current efficiency of 17.3 cdA^{-1} and maximum luminous efficiency of 8.86 lmW^{-1} at a current density of 1 mA cm^{-2}. The small-molecule based emitting layers are codoped with blue and orange phosphorescent dyes. We show that the presence of CsF/Al at cathodes not only improves electron transport in oxadiazole-containing electron transport layers (ETLs), but also facilitates electron injection through the reacted oxadiazole moiety to reduce interface resistance, which results in the enhancement of current efficiency. By selecting oxadiazole-based materials as ETLs with proper electron injection layer (EIL)/cathode structures, the brightness and efficiency of white PHOLEDs are significantly improved.

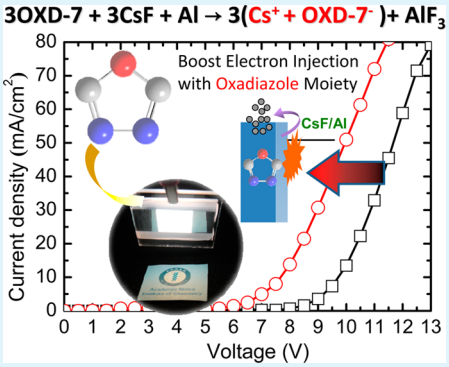

KEYWORDS: *OXD, interface, CsF/Al, PHOLED, oxadiazole, white PHOLED*

1. INTRODUCTION

With the rapid development of organic light-emitting diodes (OLEDs) in the past decade, the organic materials used in the devices, such as dopants and hosts, electron injection layers (EILs), and electron transport layers (ETLs), are becoming critical factors for optimizing the device performance. Among OLEDs, phosphorescent devices are enormously promising due to their nearly 100% internal quantum efficiency for harvesting both singlet and triplet excitons.[1,2] Proper design of phosphorescent host materials has been very important for device performance, especially the host materials for blue phosphorescent OLEDs, which must possess high triplet state energies and wide band gaps. In order to reduce fabrication time and cost and to enable large-area fabrications, solution processes for OLEDs are a promising approach, as opposed to vapor-deposition processes which require high manufacturing costs and complexity.[3−5] Only a few small molecule materials, which have high solubility and high glass transition temperature (not easily crystallized), could be used in solution process. Therefore, the design of small molecule materials used for solution process is more difficult than that for vapor-deposition process.

Polymeric materials are well known to form excellent amorphous thin films via solution-based coating, and, as a result, polymer light-emitting diodes (PLEDs) have been generally fabricated using solution processes. Only a few small-molecule (nonpolymeric) materials are used in fabricating OLEDs via solution processes because most of these materials do not condense into uniform amorphous films from solutions.[6−9] But small-molecule organic materials possess many advantages, such as higher mobility and ease of synthesis and purification.[10,11] More importantly, small-molecule-based devices would exhibit better reproducibility due to less chain entanglement, which is a typical problem with polymeric materials.[11]

For single-layer PLEDs, poly(*N*-vinylcarbazole) (PVK) has been popularly used as a host for phosphorescent or fluorescent devices.[12−29] Some other hosts are also used to fabricate PLEDs.[30,31] Much effort has been made to replace PVK and to improve PLED efficiency. For example, a dendritic host H2, 1,4-bis{3′,6′-bis[3″,6″-bis(3‴,6‴-di-*tert*-butyl)-9″H-carbazol-9″-yl)]-9′H-carbazol-9′-yl}benzene, with high triplet-state energy (2.89 eV) was synthesized to replace PVK (2.5 eV),[32,33] resulting in the highest efficiency of PLEDs to date.[34] However, for small-molecule-based devices with a

Received: June 28, 2013
Accepted: October 18, 2013
Published: October 18, 2013

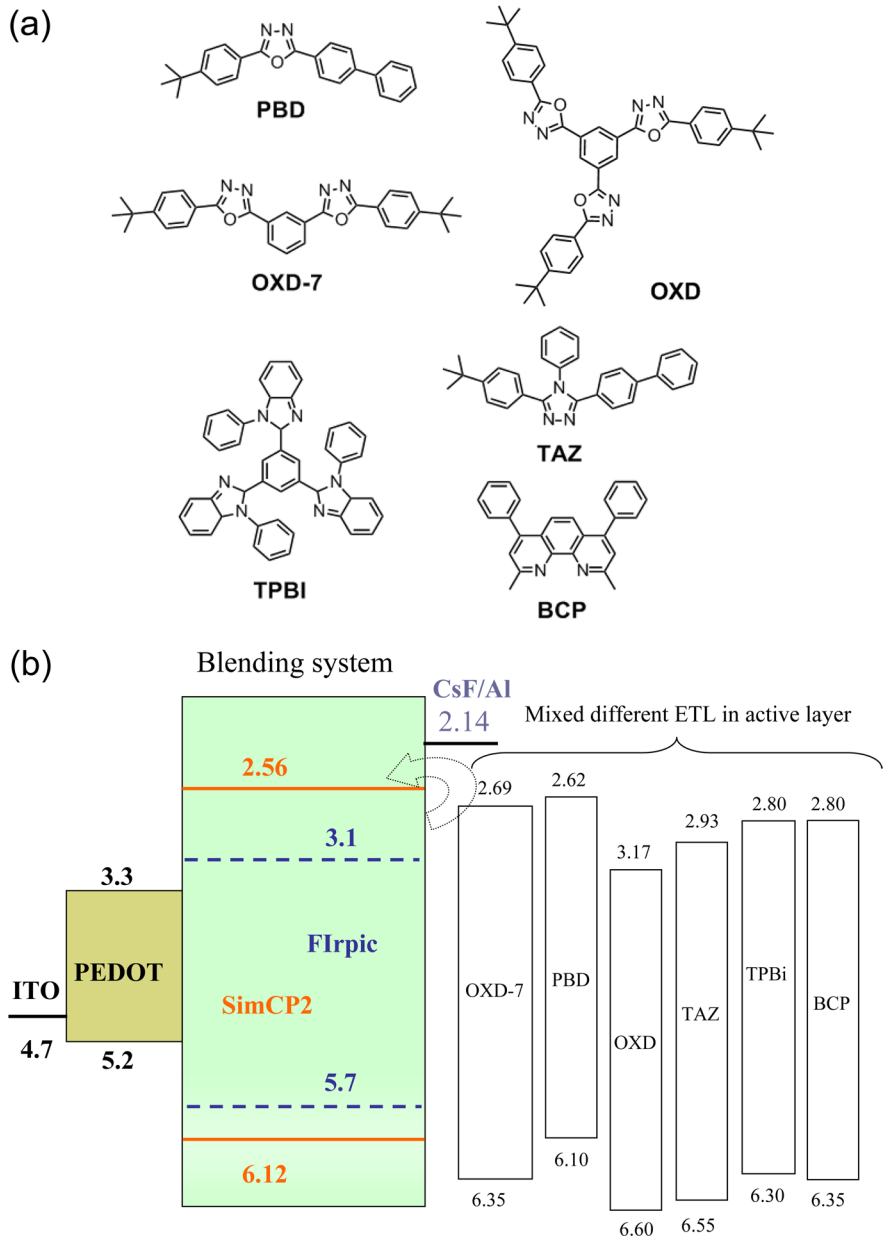

Figure 1. (a) Six kinds of ETL material structures and (b) energy level diagram for different ETLs (OXD-7, PBD, OXD, TAZ, TPBi, and BCP) blended with SimCP2 and FIrpic in OLEDs.

single-active-layer solution process, only a few reports present high-performance devices.[6−8]

We previously reported the newly synthesized 3,5-di(9H-carbazol-9-yl)tetraphenylsilane (SimCP2) as a small-molecule host material for efficient blue phosphorescent devices via a single-active-layer solution process, with a maximum current efficiency of 14.7 cdA^{-1} and luminous efficiency of 8.39 lmW^{-1}. To achieve even higher efficiencies for solution-processed devices, multilayer structures can be employed. For example, hole or exciton blocking layers have been applied using vacuum vapor deposition on the active layers to improve device performance,[8,34−43] but this leads to complexity of device fabrication.

In order to deal with the lack of electrons and low carrier mobility, which is the major problem of small molecule OLEDs fabricated by solution processes, the proper design of electron transport structures is one of the key factors to improve device efficiency. Blending the ETL with the host could be one solution. In most organic conducting materials, oxadiazole-based molecules have been widely used as good electron-transporting and hole-blocking materials to improve charge balance.[44,45]

Due to the strong electron-withdrawing effect of pentagonal ring structures, there are several benefits associated with oxadiazole moieties in the molecules, such as stable thermal properties[46,47] and the tenability of the charge carrier mobility of attached materials.[48−50] Several oxadiazole-based materials, 2-(4-biphenyllyl)-5-(4-*tert*-butylphenyl)-1,3,4-oxadiazole (PBD) and 1,3-bis[(4-*tert*-butylphenyl)-1,3,4-oxadiazolyl]-phenylene (OXD-7), for example, have been widely introduced as electron-transporting materials for green/red and blue phosphorescent OLEDs, respectively.[45,51] However, the mechanisms that enable oxadiazole-based materials to function as good ETLs are not understood. For example, as compared to 3-

(4-biphenyl)-4-phenyl-5-*tert*-butylphenyl-1,2,4-triazole (TAZ), 1,3,5-tris (*N*-phenylbenzimidazol-2-yl)-benzene (TPBi), and 2,9-dimethyl-4,7-diphenyl-1,10-phenanthroline (BCP), OXD-7 has smaller triplet state energies or lower electron carrier mobility; however, devices with OXD-7 in ETLs show much better performance than similar devices with aforementioned ETLs.[18] Furthermore, although it is quite common in OLED fabrication to include alkali metal compounds as EILs, the interactions of cathode metals, alkali-based EILs, and oxadiazole-based ETLs have not been investigated so far.

To clarify whether the interactions of cathodes, alkali compounds, and oxadiazole-based materials play an important role in device performance, electronic structures and interfacial chemical reactions were investigated theoretically with quantum chemistry calculations, as well as experimentally via current density versus voltage (J–V) characteristics and ultraviolet and X-ray photoemission spectroscopy (UPS and XPS). We found that the reactions between the oxadiazole-based molecules, alkali EILs, and Al cathode are key factors in boosting electron injection. Based on the aforementioned results, we demonstrate high-efficiency white phosphorescent OLEDs by codoping blue and orange phosphorescent dyes into emitting layers using single-active-layer solution-based processes, with current efficiency of 17.3 cdA^{-1} and maximum luminous efficiency of 8.86 lmW^{-1} at a current density of 1 mA cm^{-2} (170 cdm^{-2}).

2. RESULTS AND DISCUSSION

2.1. Device Characteristics with Various ETLs. Small molecular host SimCP2 possesses an ambipolar characteristic, with relatively high hole and electron mobility, both around 1–3 × 10^{-4} cm^2 V^{-1} s^{-1}.[10] In general, it is harder to find suitable ETLs for blue phosphorescent doping systems than for green and red doping systems because of their wider band gap and higher triplet states. To optimize device performance, six different ETL materials, that is, 2-(4-biphenyllyl)-5-(4-*tert*-butylphenyl)-1,3,4-oxadiazole (PBD), 1,3,5-tris[(4′-*tert*-butylphenyl)-1,3,4-oxadiazolyl]benzene (OXD), 1,3-bis[(4-*tert*-butylphenyl)-1,3,4-oxadiazolyl]phenylene (OXD-7), 3-(4-biphenyl)-4-phenyl-5-*tert*-butylphenyl-1,2,4-triazole (TAZ), *N*-arylbenzimidazoles (TPBi), and 2,9-dimethyl-4,7-diphenyl-1,10-phenanthroline (BCP), with various energy levels (HOMO and LUMO), triplet state energies, electron mobility, and molecular structures, were studied. Among them, PBD, OXD, and OXD-7 contain oxadiazole moieties, while the other three materials do not. The molecular structures and energy bands of these molecules are shown in Figure 1.

With respect to the vacuum level, the energy levels of the HOMOs among these materials are around 6.10–6.60 eV while the energy levels of the LUMOs are around 2.62–3.17 eV, which is a relatively large disparity. All the values of band gap and HOMO are determined from our measurements of absorbance and UPS and the values of LUMO are calculated by subtracting the band gap from the HOMO, as shown in Figure 1 and Table 1. The work function of the EIL/cathode used in this study is around 2.14 eV, much higher than all the values of LUMOs. The triplet state energies (T_1) of OXD-7, PBD, OXD, TAZ, TPBi, and BCP are 2.7, 2.46, 2.7, 2.8, 2.65, and 2.6 eV, respectively,[18,23,52] so the proper materials for phosphorescence are OXD-7, OXD and TAZ due to their relatively high triplet state energy, especially TAZ. For carrier mobility concerns, the electron mobilities of OXD-7, PBD, OXD, TAZ, TPBi, and BCP are 1-4 × 10^{-5}, 8 × 10^{-7}, 1.2 × 10^{-6}, 1–3 × 10^{-5}, 3–8 × 10^{-5}, and 1.1 × 10^{-3} cm^2 V s^{-1}, respectively.[9,52−54] We list the characteristics of triplet state energy (T_1), energy band gap (E_g), and carrier mobility (μ_e) for these materials in Table 1.

Table 1. Triplet State Energy (T_1), Energy Band Gap (E_g), and Carrier Mobility (μ_e) for Six Different ETL Materials

	OXD-7	PBD	OXD	TAZ	TPBi	BCP
T_1 (eV)	2.70	2.46	2.70	2.80	2.65	2.60
E_g (eV)	3.66	3.48	3.43	3.62	3.50	3.55
μ_e (cm^2 V s^{-1})	1–4 × 10^{-5}	8 × 10^{-7}	1.2 × 10^{-6}	1–3 × 10^{-5}	3–8 × 10^{-5}	1.1 × 10^{-3}

Six devices having ETLs with 30% OXD-7, PBD, OXD, TAZ, TPBi, and BCP mixed into their active layers were fabricated and studied. The current density and luminance versus voltage are shown in Figure 2. As far as material characteristics are concerned, TAZ has the highest triplet state energy among these ETL materials, and its electron mobility approximates that of OXD-7.[53] Therefore, we would expect that using TAZ would result in better performance. In addition, the electron mobility of BCP is almost 80 000; 1000 times higher than that of PBD or OXD. However, the devices with OXD-7, PBD and OXD demonstrate much higher currents than the devices with TAZ, TPBi, and BCP. The oxadiazole-based ETLs possess the worst electron mobility, but they demonstrate very good electrical characteristics. The luminance also shows an unexpected result. Despite the relatively low triplet state energy of PBD (2.46 eV), the device with these molecules demonstrates higher luminance than the devices blending TAZ (2.8 eV), TPBi (2.65 eV), and BCP (2.6 eV). In this investigation, the devices with oxadiazole-based ETLs exhibit better performance in terms of current density and luminance, even through these materials have lower electron mobility and somewhat lower triplet state energies. These results suggest that the superior performance of the oxadiazole-based devices tested in this study might not be due to the material characteristics of the ETLs themselves, but because of the interfacial properties of the organic layers and cathodes. Therefore, the interfacial chemical and electronic interactions were investigated through in-situ XPS and UPS.

2.2. X-ray Photoemission Spectroscopy and Interfacial Chemistry. Figure 3 shows the evolution of XPS spectra with the incremental deposition of Al and CsF (16 Å) on OXD-7 surfaces. As shown at the bottom of Figure 3a, the binding energy of the carbon 1s core level for pristine OXD-7 is observed at two different values of 284.7 eV and 287.4 eV owing to the presence of benzene and oxadiazole moieties in OXD-7. The intrinsic binding energies of nitrogen 1s, as shown at the bottom of Figure 3b, and the oxygen 1s core level, as shown at the bottom of Figure 3c, for pristine OXD-7 are about 399.2 and 534.7 eV, respectively.

To investigate the interfacial interactions, we further evaporate CsF at a low rate of 0.03 nm/s to form a 16 Å thick CsF layer on OXD-7. The deposition of CsF on OXD-7 leads to a considerable variance in XPS spectra that can be clearly observed in Figure 3. XPS spectra of both the nitrogen and oxygen 1s core levels split into two peaks after CsF deposition, which indicates that the electronic structures of both nitrogen and oxygen have been changed with the presence of CsF molecules. According to the XPS spectra shown in Figure 3b, the original peak of the nitrogen 1s core level at 399.2 eV shifts toward higher binding energy by 0.8 eV, while an additional peak appears at 398.0 eV. Similarly in Figure 3c,

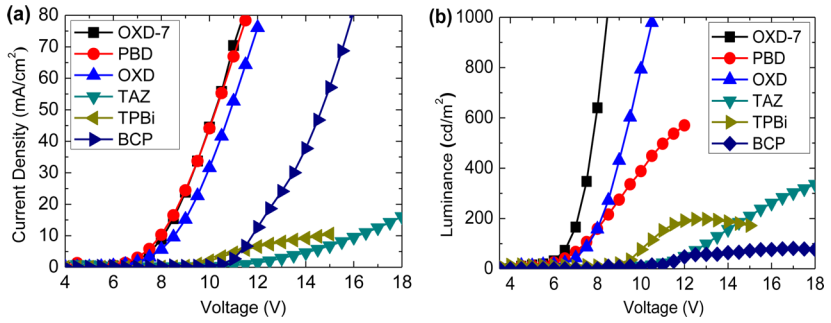

Figure 2. These devices blend 30% of different ETLs into the active layer for a single-layer solution-processed blue PHOLED. (a) Current density versus voltage. (b) Luminance versus voltage for blue PHOLEDs in the forward direction.

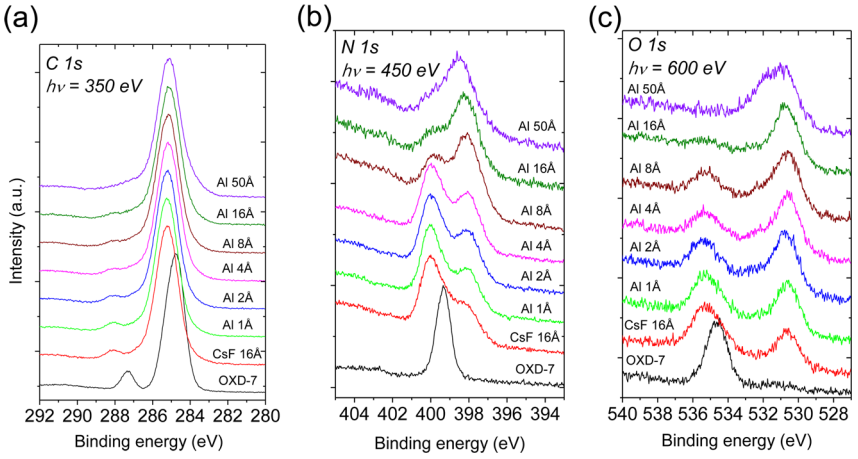

Figure 3. XPS spectra of incremental deposition of Al onto a 16 Å thin film of CsF deposited on bulk OXD-7. a) XPS spectra of carbon 1s core level, b) XPS spectra of nitrogen 1s core level, c) XPS spectra of oxygen 1s core level.

the original peak of the oxygen 1s core level at 534.7 eV shifts 0.8 eV toward higher binding energy, with an additional peak at 530.6 eV.

On the other hand, for the XPS spectrum of the carbon 1s core level in Figure 3a, the peak at the lower binding energy, associated with the carbon atoms in the benzene moiety, merely shifts from 284.7 to 285.5 eV, while the one with higher energy, associated with the carbon atoms in the oxadiazole moiety, not only shifts but also is attenuated in magnitude. For the carbon atoms in the oxadiazole moiety, the electronic configuration of carbon does not undergo a split of its core-level spectrum as observed in the nitrogen and oxygen 1s core level spectra. Since all the photoemission spectra shown in this study are in reference to the Fermi level, the constant 0.8 eV shifts observed in all XPS core level spectra (as well as in the UPS valence band spectra, not shown in this report) indicate the upward shift of the Fermi level in band gaps and the n-type doping effect in the organic molecules. The additional peaks observed at relatively low binding energies in both nitrogen and oxygen XPS spectra can be regarded as different electronic configurations, with more electrons surrounding oxygen and nitrogen atoms in OXD-7 with CsF than those in pristine OXD-7, which indicates the electron distribution with CsF deposited on OXD-7.

In addition, XPS spectra of the fluorine 1s core level are measured as additional evidence for CsF interacting with the oxadiazole moiety and are shown in Figure 4. There is a dissimilarity between the two materials that CsF is deposited on, that is, OXD-7 and a pre-cleaned Au substrate. In the case of CsF on OXD-7, as shown at the bottom Figure 4c, the binding energy of the fluorine 1s core level is located at 682.7 eV, which is 1 eV lower than that of CsF on Au as shown at the bottom of Figure 4a. This dissimilarity indicates again that charge redistribution takes place when CsF contacts oxadiazole, since the pristine XPS spectrum of fluorine 1s for CsF on Au substrates can be used as a comparison, assuming no interaction between CsF and Au.[55]

These observations imply that some interactions, such as chemical reactions and charge exchanges, exist between CsF and oxadiazole moieties, leading to the variance of the OXD-7 electronic structure. To further clarify the evolution of oxadiazole moieties with CsF molecules, we theoretically investigate the electronic distribution of OXD-7 and OXD-7/CsF with energy and geometry optimization through quantum chemistry calculations. The crystallographically obtained structure is used as an initial condition for all computations, and subsequent optimization is performed using the Density Functional Theory (DFT) method.

2.3. Numerical Simulation Based on Density Functional Theory (DFT) Method. Figure 5a and b shows the electronic configuration of the HOMO and LUMO of a pristine OXD-7 molecule, respectively. Molecular orbital formation in the presence of CsF gives a hint that a chemical interaction has been involved as shown in Figure 5c. According to Figure 5c, cesium atoms are attracted by OXD-7 due to the electron-deficient properties of the oxadiazole moiety, which causes charge exchange between cesium and the nitrogen in the oxadiazole moiety; this results in the n-type doping effect shown in the UPS and XPS spectra. With the formation of the

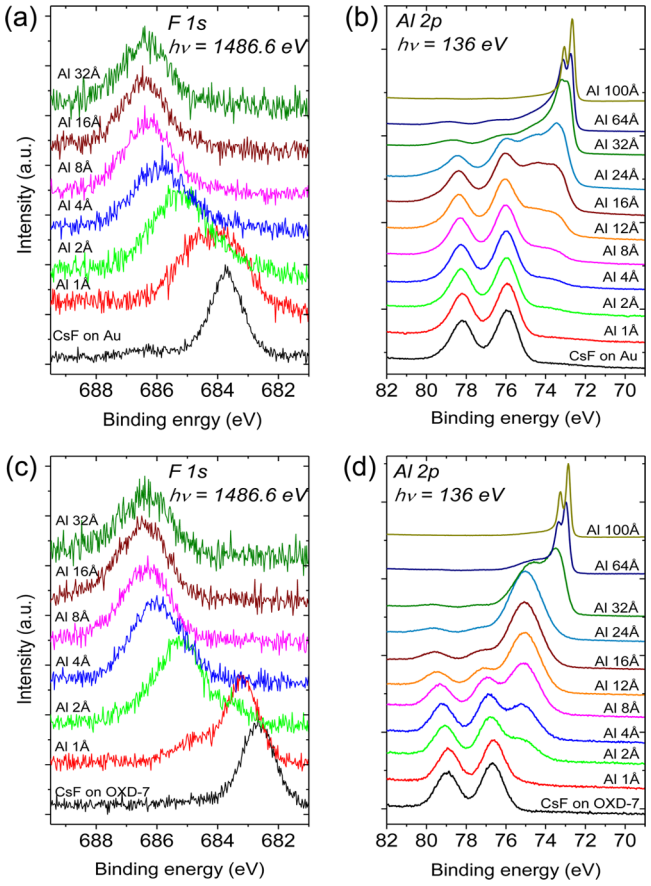

Figure 4. XPS spectra of incremental deposition of Al onto a 16 Å thin film of CsF deposited on (a,b) Au and (c,d) OXD-7. The left-hand side corresponds to XPS spectra of the fluorine 1s core level, and the right-hand side corresponds to XPS spectra of the aluminum 2p core level.

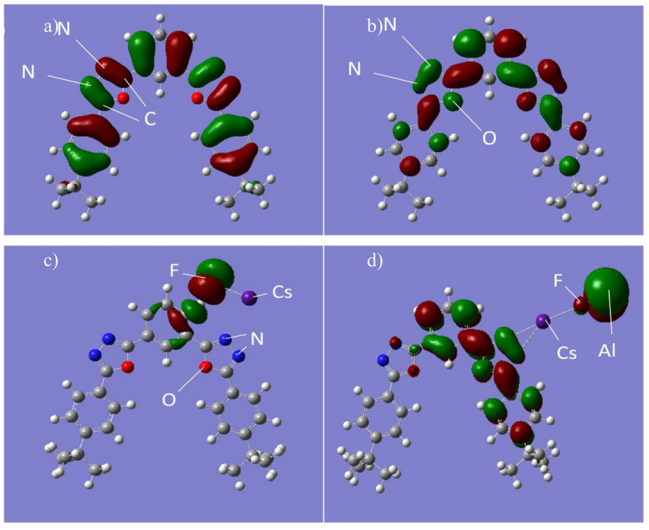

Figure 5. Optimal geometry structures and electronic configurations of (a) HOMO of OXD-7 molecule, (b) LUMO of OXD-7 molecule, (c) HOMO of Cs-OXD metal complex, and (d) HOMO of Al-F-Cs-OXD complex.

Cs-OXD complex, the structure of CsF tends to change since the bond between cesium and fluorine has been weakened as soon as a hydrogen bond is formed between fluorine and hydrogen in the benzene moiety. The electron density around fluorine hence increases and consequently induces high polarity within the molecule, which leads to a lower binding energy of the fluorine 1s core level as observed at the bottom of Figure 4c, when compared to that of pristine CsF at the bottom of Figure 4a. However, the oxygen in oxadiazole may not bond with cesium because the required Gibbs free energy of formation is too large to form a stable metal complex without compromising the OXD-7 structure.

Following the deposition of CsF, the cathode material, aluminum, is incrementally deposited onto the CsF thin film in all the cases aforementioned, to obtain the evolution of a Cs-OXD complex interacting with Al. The evolutions of XPS spectra of carbon 1s, nitrogen 1s, and oxygen 1s are shown in Figure 3, and the evolutions of XPS spectra for fluorine and aluminum are shown in Figure 4. Similarly, the electronic configuration for OXD-7, CsF, and Al is also carried out theoretically in Figure 5d to determine the mechanism of molecular interactions causing enhanced efficiency in device performance. As shown in Figure 3, the peaks at the lower binding energy of both the nitrogen and oxygen 1s core levels, which correspond to the oxadiazole moieties affected by cesium atoms as mentioned above, grow gradually with the increase of Al thickness. Contrary to the growth of Cs-OXD complex components, the intensity decline of peaks at higher binding energies of both oxygen 1s and nitrogen 1s core levels implies that fewer pristine oxadiazole moieties exist with the presence of Al at the surface, and the proportion of the Cs-OXD complex increases. The evolution of the carbon 1s core level relating to the oxadiazole moiety reveals the same results. This is because incorporating thermally evaporated Al with CsF would dissociate CsF and thus release cesium atoms into the organic layer with the generation of AlF_3.[55−57]

To verify this chemical reaction between Al and F, the evolution of the interface component is investigated via XPS with incremental Al deposition, as shown in Figure 4. When aluminum is initially deposited on CsF/OXD-7, the binding energy of the aluminum 2p core level is at a higher value, 74.9 eV, than that of pure aluminum, which implies that aluminum atoms are losing electrons to form aluminum ions. With more aluminum deposition, the binding energy of the aluminum 2p core level is still observed at the same energy position until the spectrum is dominated by the spin-orbit splitting peak of pristine aluminum with aluminum deposition over 24 Å, which means that Al atoms deposited at the CsF/OXD-7 interfaces have been totally converted into aluminum ions. On the other hand, the aluminum 2p core level shows simultaneous growth of aluminum ions and pristine aluminum when aluminum is incrementally deposited on CsF/Au.

To further clarify the role of aluminum ions, which might be involved in the chemical interaction with fluorine ions owing to the high polarity of the hydrogen bond formed between benzene and fluorine, the evolution of the fluorine 1s core level shown in Figure 4 should be considered. Although the initial locations of the fluorine 1s core level in the two cases, CsF deposited on OXD-7 and on gold substrate, are at different binding energies due to the aforementioned formation of a Cs-OXD metal complex, the binding energy of the fluorine 1s core level in either of the two cases shifts gradually toward higher binding energies to the same value of 686.4 eV, with the deposition of Al. The results indicate the formation of AlF_3, since fluorine ions would form a relatively strong ionic bond

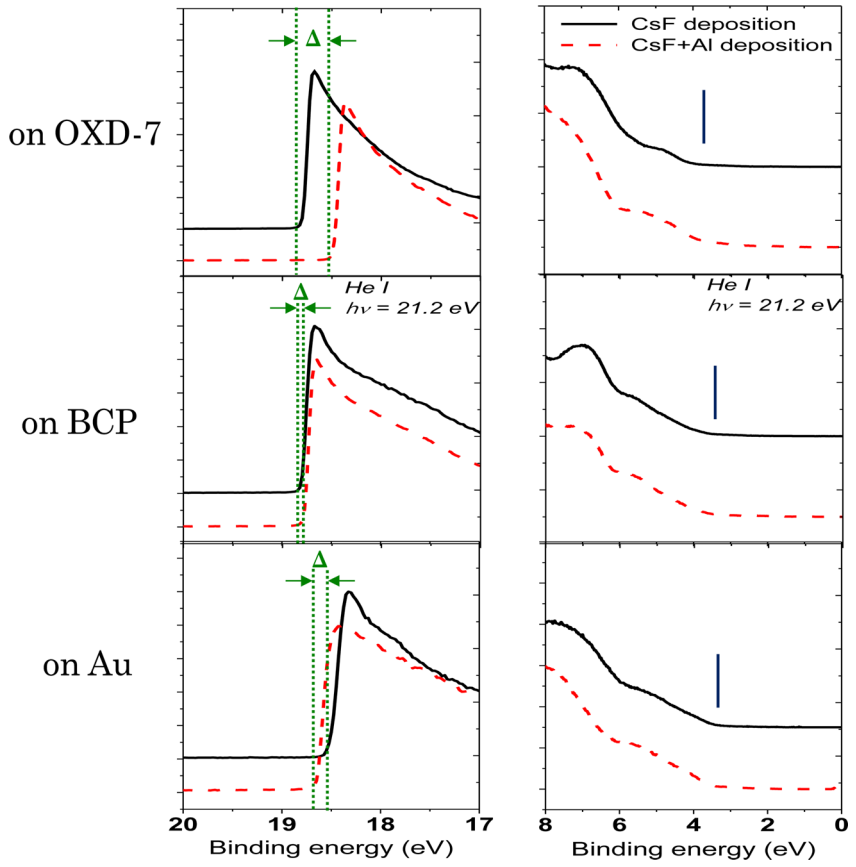

Figure 6. UPS spectra of 16-Å-thick CsF on different bulk materials. The left-hand side shows the shift (Δ) of the cutoff after Al deposition, and the right-hand side corresponds to the HOMO region.

with aluminum, which would make the fluorine 1s core level shift toward higher binding energy.

To verify this point, we carry out the molecular simulation further and investigate the molecular orbital formation of the Cs-OXD metal complex with the presence of aluminum as shown in Figure 5d. It confirms that the expected Al−F bonding is formed, and the Cs atom is tightly captured by the oxadiazole moiety, which indicates that a large amount of Cs-OXD metal complex would be generated and lead to effective n-doping of OXD-7 at the interfaces of Al/CsF cathodes. Accordingly, a lower contact resistance between the Al cathode and OXD-7 can be achieved and electron injection efficiency is improved with the existence of the Al-F-Cs-OXD complex. Moreover, improvement in electron transport of an OXD-7 device can also be understood by evaluating the similarity in electron configuration between the HOMO level of Al-F-Cs-OXD complex and the LUMO level of pristine OXD-7. According to the concept of *reorganization energy*, a reaction seems likely to take place if the electron configuration of products is highly similar to that of reactants. By comparing the HOMO of the Al−F−Cs-OXD complex with the LUMO of pristine OXD-7, Figure 5b and d shows that the electron configuration of the oxadiazole moiety in both cases is highly similar, which means that less reorganization energy is needed for electron redistribution. From another viewpoint, the similarity between these two molecular orbitals represents a large overlap of electron wave functions when calculating the interaction cross-section, leading to higher probability of electron transition. Therefore, an electron transported between individual Al-F-Cs-OXD complexes can reach the LUMO of the adjacent complex and travel in the film without disturbing the initial electron configuration. The overall reaction among OXD-7, CsF, and Al should be

$$3\text{OXD-7} + 3\text{CsF} + \text{Al} \rightarrow 3(\text{Cs}^+ + \text{OXD-7}^-) + \text{AlF}_3 \quad (1)$$

and the calculated Gibbs free energy for this process is negative, which means such a reaction is energetically favorable.

For comparison, we also carry out photoemission spectroscopy analysis and theoretical simulation of the interaction between other ETL materials, such as BCP, and CsF/Al, to check if similar reactions occur. Both simulated electron configurations and experimental XPS spectra of BCP incorporated with CsF/Al show results different from those in the OXD-7 case, which means that the improvement of both electron injection and transport might be due to the interaction of oxadiazole-based materials with CsF/Al cathodes.

2.4. Ultraviolet Photoemission Spectroscopy and the HOMO Energy Levels. To understand the influence of the interface between the ETL and CsF/Al cathodes on electron transport at the interface, valence electron energy levels are also investigated with UPS. As shown in Figure 6, with Al deposition it seems there is no change whatsoever in the HOMO position of the interfaces of CsF with OXD-7, BCP, and Au. However, the secondary cutoff reveals large differences among these three interfaces.

With Al deposition, the cutoff of CsF/OXD-7 exhibits a remarkable shift in binding energy due to the charge-exchange-induced interface dipole among molecules, while there is no such change observed in the UPS spectra of either the CsF/

BCP or the CsF/Au interface. Furthermore, the deposition of Al directly on pristine OXD-7 was also investigated and the results indicated that there is no charge exchange or interaction between Al and OXD-7 without the present of CsF. These investigations indicate that inefficient electron injection can be attributed to the lack of chemical interaction between dopant and electron-transporting material even though the band alignment within the OLED is well-matched. On the other hand, incorporating oxadiazole-containing material with an alkali metal compound and an Al cathode can produce an efficient phosphorescence, based on the promotion of intersystem crossing with spin-orbital coupling by the introduction of the transition metal dopant, to enhance brightness.

2.5. Optimization of White-Light OLEDs. To validate that interaction of oxadiazole moieties with CsF/Al would facilitate electron injection, devices (having ETLs with 30% OXD-7) with different EIL/cathode structures, CsF/Al, CsF/Ag, CsF/Al (10 nm)/Ag, Al, and Ag, are analyzed. In the case of CsF/Al/Ag, the thickness of Al is only 10 nm in order to check if the interfacial reaction of CsF and oxadiazole with Al is the key to the improvement of device performance. Indeed the two cases of CsF/Al and CsF/Al (10 nm)/Ag exhibit the same electrical characteristics and luminance, much better than those of others shown in Figure 7. This demonstrates that the

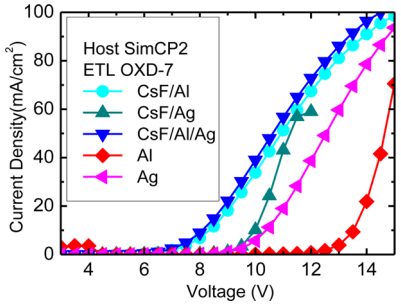

Figure 7. Current density versus voltage for the device with 30% OXD-7 blended ETL, deposited EIL of 2 nm (with and without CsF), and cathode of 100 nm (Al and Ag). The thicknesses are CsF (2 nm)/Al (10 nm)/Ag (100 nm).

incorporation of oxadiazole-based ETLs with CsF/Al cathode structures results in excellent current injection efficiency through the chemical interaction described in the previous section.

In order to further understand the role of oxadiazole-based material in these devices, we compare the similar devices with and without OXD-7, as shown in Figure 8. Without OXD-7, the device indeed has lower current density due to poor electron injection, leading to high turn on voltages and extremely worse luminance. The aforementioned interaction between oxadiazole-based material and CsF/Al plays a key role for the improvement of the devices in this study.

Using this effective cathode structure with the high-efficiency solution-processed blue phosphorescence OLED (PHOLED) we reported previously,[58] we are able to demonstrate high efficiency small-molecule based white PHOLEDs with a single-active-layer solution process. Based on the blue PHOLEDs with FIrpic doped SimCP2, the red-orange phosphorescent dopant Ir(2-phq)$_3$ is added into the active layer to generate a white PHOLED. The photoluminescence peak of Ir(2-phq)$_3$ doped in SimCP2 is around 584 nm. The total dopant concentration is

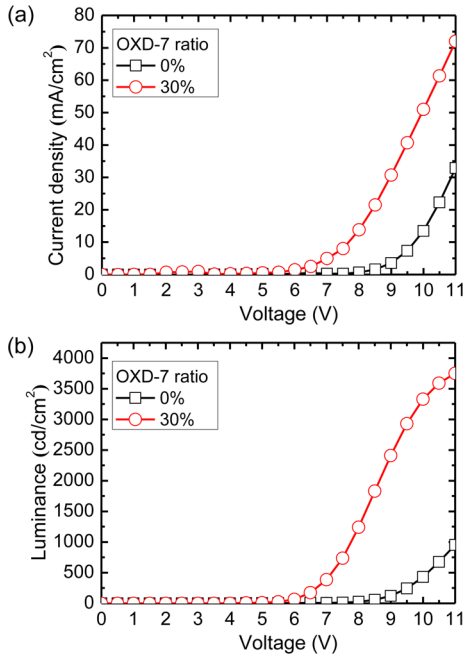

Figure 8. (a) Current density versus voltage and (b) luminance versus voltage of the similar devices with and without OXD-7 in the active layer. The device structures are similar to those shown in Figure 2.

6%, and the FIrpic:Ir(2-phq)$_3$ ratio is kept at 74:1. As shown in Figure 9a, the maximum current efficiency is 17.3 cdA^{-1} and the maximum luminous efficiency is 8.86 lmW^{-1} at a current density of 1 mAcm^{-2} (170 cdm^{-2}) for the small-molecule based white PHOLED with a single-active-layer solution process. The EL spectra of the white PHOLED are shown in Figure 9b. The three peaks are at 476, 500, and 576 nm, respectively. The EL peak of 475 nm of FIrpic is decreased due to stronger absorption of Ir(2-phq)$_3$ and it raises the "shoulder" at 500 nm at the same time. The white PHOLEDs in this study exhibit a CIE coordination of (0.34, 0.43) and a CRI of 65. A picture of a white PHOLED with large area of 1 × 1 cm^2 is shown in Figure 9c.

3. CONCLUSION

In conclusion, we demonstrate a high-efficiency small-molecule-based white PHOLED produced using a single-active-layer solution process. We show that the presence of CsF/Al not only improves electron transport in oxadiazole-containing ETLs, but also facilitates electron injection through the reacted oxadiazole moiety to reduce interface resistance, which results in the enhancement of current efficiency. By selecting oxadiazole-based materials as ETLs with proper EIL/cathode structures, the brightness and efficiency of white PHOLEDs are significantly improved and reach a record high. Moreover, theoretical results and XPS and UPS spectra give clear evidence of the superiority of the oxadiazole moiety in generating effective doped conducting ETLs more efficiently. Accordingly, for high-efficiency solution-processed small-molecule OLEDs, it is extremely important to use CsF as the EIL and an oxadiazole-containing electron-transporting material specifically chosen to interact with the dopant to reach an effective n-type doping in the ETL. As a result, a white PHOLED with a current efficiency of 17.3 cdA^{-1} and the maximum luminous efficiency of 8.86 lmW^{-1} was achieved.

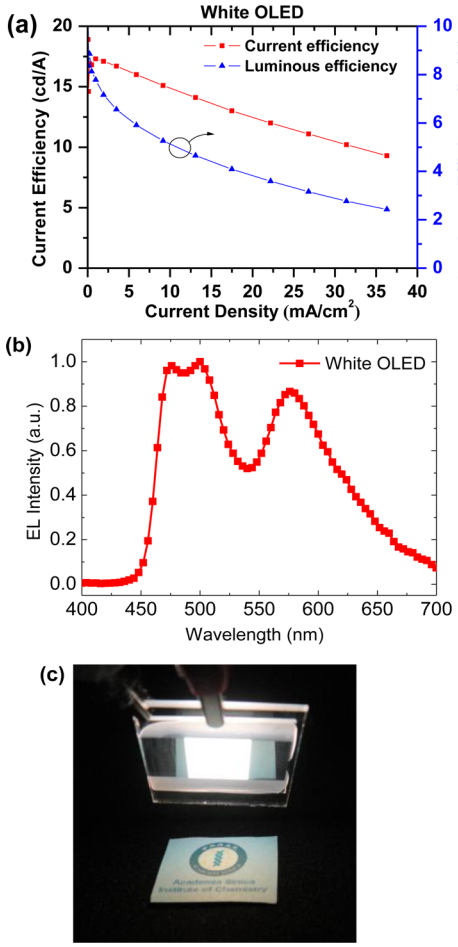

Figure 9. Total dopant amount fixed at 6% for the white PHOLED. The ratio of FIrpic and $Ir(2\text{-phq})_3$ is fixed 74:1. (a) Current (cdA^{-1}) and luminous efficiency (lmW^{-1}) versus current density of SimCP2-based OLEDs. (b) EL spectra normalized at λ_{max}^{EL} for the white PHOLED. (c) White PHOLED with large area of 1 × 1 cm^2.

4. EXPERIMENTAL SECTION

Materials. Iridium tin oxide (ITO) substrates with a thickness of 100 nm and sheet resistance around 25 Ω/sq were purchased from Merck. Poly(3,4-ethylenedioxythiophene) (PEDOT) doped with poly(styrenesulfonate) (PSS) (CH8000) was purchased from Sigma-Aldrich. The PBD, TAZ, BCP, and OXD-7 as ETLs, and FIrpic as blue phosphorescent dopants are were purchased from either Sigma-Aldrich or Lumtec Corp. The ambipolar small molecule host, SimCP2, and electron transport materials, OXD and TPBi, were synthesized in the laboratory according to a procedure reported previously.[10,59]

General Method. The structures of the OLEDs investigated in this study are shown in Figure 1a. The ITO substrates were precoated with PEDOT:PSS and then baked in the air at 150°C for 10 min. Blends of SimCP2, the selected ETL (OXD-7, PBD, OXD, TAZ, TPBi, or BCP), and FIrpic dissolved jointly in chlorobenzene were spin-coated on PEDOT:PSS-covered ITO substrates. The active layer was then annealed at 90°C for 30 min. After spin-coating, cathodes with an ultrathin CsF (2 nm) interfacial layer on silver or aluminum (100 nm) were deposited in a thermal-evaporation vacuum chamber. For our solution-processed single-active-layer blue PHOLED, the mixing weight percentage of the host SimCP2, selected ETL (OXD-7, PBD, OXD, TAZ, TPBi, and BCP), and FIrpic was 65, 30 and 5%, respectively. For the white PHOLED, the mixing weight percentage of the host SimCP2 and ETL OXD-7 were 64% and 30%. The total dopant was 6% including sky-blue dopant FIrpic and red-orange dopant $Ir(2\text{-phq})_3$. The FIrpic:$Ir(2\text{-phq})_3$ ratio was kept at 74:1.

Thicknesses of all organic and metal layers were calibrated by a surface profiler (Dektak 150 Veeco). The devices were hermetically sealed with glass and UV resins in a glove box (O_2 and H_2O concentration below 0.1 ppm) after the deposition of cathodes. A device with an emissive area of 0.04 cm^2 was defined by a shadow mask in the deposition chamber. The characteristics of voltage-current density were measured by a DC current/voltage source meter (Keithley 2400), and the device electroluminance (cdm^{-2}) was monitored with a spectrophotometer (PR650; Photo Research).

Photoemission experiments were obtained in three interconnected ultrahigh vacuum chambers, two deposition chambers for metal and organic thermal evaporation, respectively, and another for spectroscopy analysis with a base pressure of about 10^{-10} Torr. By measuring the photoemission spectra on a gold film cleaned by Ar sputter, the Fermi level of the system could be obtained.[1,2,60,61] Through thermal evaporation in the deposition chambers, all organic materials, CsF, and metal were deposited sequentially and were transferred in situ into the analysis chamber. In particular, the CsF source needed to be degassed thoroughly at the temperature around its sublimation point for 15 min to remove probable contamination absorbed in ambient conditions. The valence band UPS were performed using He I (21.2 eV) and He II (40.8 eV) photon lines as excitation sources, and the photoelectrons were analyzed with a hemispherical analyzer with an overall resolution of 0.05 eV. To get a better resolution, XPS was also performed at the National Synchrotron Radiation Research Center (NSRRC), Hsinchu, Taiwan, R.O.C. The high-brightness photon beam was provided by the MAGM(BL08B) with photon energies in the range of 300 to 1000 eV. The core level spectra were measured with photon energies chosen to optimize the signal-to-noise ratio.

Optimization of Molecular Geometry and Electronic Configuration. In this work, molecular dynamics and the electronic structure of organic materials were optimized via common DFT methods,[62,63] such as B3LYP.[64] In general, B3LYP is a semi-empirical hybrid method from DFT which gives high accuracy for molecular computation. All optimization by the B3LYP method in this work was performed using a quantum-chemical calculation package, Gaussian 03 (Gaussian, Inc.), with a 6-31G(d,p) basis set while a LANL2DZ[65] basis set was considered in case of the presence of heavy atoms such as cesium. To make the complicated molecular system solvable, a pseudopotential approximation was also included to deal with the relativistic effect induced by the heavy atoms. In this way, the molecular orbitals calculated through the B3LYP exchange correlation function could be obtained.

■ ASSOCIATED CONTENT

Supporting Information

AFM images of devices with various ETL dopant. This material is available free of charge via the Internet at http://pubs.acs.org.

■ AUTHOR INFORMATION

Corresponding Authors

*E-mail: cchen@chem.sinica.edu.tw.
*E-mail: chihiwu@cc.ee.ntu.edu.tw.

Author Contributions

‖Y. T. Chang and J. K. Chang contributed equally to this work.

Notes

The authors declare no competing financial interest.

■ ACKNOWLEDGMENTS

The authors would like to thank Dr. Ing-Shouh Hwang, Dr. En-Te Hwu, and Wei-Min Wang of the Institute of Physics, Academia Sinica, for measuring surface morphologies of thin films by atomic force microscopy (AFM). This work is financially supported by National Science Council (NSC 101-2628-M-002-004-MY3 and NSC 101-2113-M-001-004-MY2)

and the Center for Emerging Materials and Advanced Devices, National Taiwan University.

REFERENCES

(1) Ding, J.; Gao, J.; Cheng, Y.; Xie, Z.; Wang, L.; Ma, D.; Jing, X.; Wang, F. *Adv. Funct. Mater.* **2006**, *16*, 575−581.
(2) Huang, W.-S.; Lin, J. T.; Chien, C.-H.; Tao, Y.-T.; Sun, S.-S.; Wen, Y.-S. *Chem. Mater.* **2004**, *16*, 2480−2488.
(3) Wu, H.; Ying, L.; Yang, W.; Cao, Y. *Chem. Soc. Rev.* **2009**, *38*, 3391−3400.
(4) Kamtekar, K. T.; Monkman, A. P.; Bryce, M. R. *Adv. Mater.* **2010**, *22*, 572−582.
(5) Gather, M. C.; Köhnen, A.; Meerholz, K. *Adv. Mater.* **2011**, *23*, 233−248.
(6) Hou, L.; Duan, L.; Qiao, J.; Li, W.; Zhang, D.; Qiu, Y. *Appl. Phys. Lett.* **2008**, *92*, 263301−263303.
(7) Jiang, W.; Duan, L.; Qiao, J.; Zhang, D.; Dong, G.; Wang, L.; Qiu, Y. *J. Mater. Chem.* **2010**, *20*, 6131−6137.
(8) Jiang, W.; Duan, L.; Qiao, J.; Dong, G.; Wang, L.; Qiu, Y. *Org. Lett.* **2011**, *13*, 3146−3149.
(9) Liu, S.-W.; Yuan, C.-H.; Yeh, S.-J.; Wu, M.-F.; Chen, C.-T.; Lee, C.-C. *J. Soc. Inf. Disp.* **2011**, *19*, 346−352.
(10) Tsuboi, T.; Liu, S.-W.; Wu, M.-F.; Chen, C.-T. *Org. Electron.* **2009**, *10*, 1372−1377.
(11) Duan, L.; Hou, L.; Lee, T.-W.; Qiao, J.; Zhang, D.; Dong, G.; Wang, L.; Qiu, Y. *J. Mater. Chem.* **2010**, *20*, 6392−6407.
(12) Song, M.; Park, J. S.; Kim, C.-H.; Im, M. J.; Kim, J. S.; Gal, Y.-S.; Kang, J.-W.; Lee, J. W.; Jin, S.-H. *Org. Electron.* **2009**, *10*, 1412−1415.
(13) Tsai, M. H.; Lin, H. W.; Su, H. C.; Ke, T. H.; Wu, C. C.; Fang, F. C.; Liao, Y. L.; Wong, K. T.; Wu, C. I. *Adv. Mater.* **2006**, *18*, 1216−1220.
(14) Zou, J.; Wu, H.; Lam, C.-S.; Wang, C.; Zhu, J.; Zhong, C.; Hu, S.; Ho, C.-L.; Zhou, G.-J.; Wu, H.; Choy, W. C. H.; Peng, J.; Cao, Y.; Wong, W.-Y. *Adv. Mater.* **2011**, *23*, 2976−2980.
(15) Wu, H. B.; Zou, J. H.; Liu, F.; Wang, L.; Mikhailovsky, A.; Bazan, G. C.; Yang, W.; Cao, Y. *Adv. Mater.* **2008**, *20*, 696−702.
(16) Chen, F.-C.; Chien, S.-C.; Chen, Y.-S. *Appl. Phys. Lett.* **2009**, *94*, 043306−043303.
(17) Hou, L.; Duan, L.; Qiao, J.; Zhang, D.; Wang, L.; Cao, Y.; Qiu, Y. *J. Mater. Chem.* **2011**, *21*, 5312−5318.
(18) Tokito, S.; Suzuki, M.; Sato, F.; Kamachi, M.; Shirane, K. *Org. Electron.* **2003**, *4*, 105−111.
(19) Liu, H.-M.; He, J.; Wang, P.-F.; Xie, H.-Z.; Zhang, X.-H.; Lee, C.-S.; Sun, B.-Q.; Xia, Y.-J. *Appl. Phys. Lett.* **2005**, *87*, 221103−221103.
(20) Mathai, M. K.; Choong, V.-E.; Choulis, S. A.; Krummacher, B.; So, F. *Appl. Phys. Lett.* **2006**, *88*, 243512−243513.
(21) Yang, X.; Müller, D. C.; Neher, D.; Meerholz, K. *Adv. Mater.* **2006**, *18*, 948−954.
(22) Choulis, S. A.; Mathai, M. K.; Choong, V.-E.; So, F. *Appl. Phys. Lett.* **2006**, *88*, 203502−203503.
(23) Suzuki, M.; Tokito, S.; Sato, F.; Igarashi, T.; Kondo, K.; Koyama, T.; Yamaguchi, T. *Appl. Phys. Lett.* **2005**, *86*, 103507.
(24) Chen, F.-C.; Yang, Y.; Thompson, M. E.; Kido, J. *Appl. Phys. Lett.* **2002**, *80*, 2308−2310.
(25) Yang, X. H.; Neher, D. *Appl. Phys. Lett.* **2004**, *84*, 2476−2478.
(26) Huang, J.; Hou, W.-J.; Li, J.-H.; Li, G.; Yang, Y. *Appl. Phys. Lett.* **2006**, *89*, 133509−133503.
(27) Hino, Y.; Kajii, H.; Ohmori, Y. *Thin Solid Films* **2006**, *499*, 359−363.
(28) Nakamura, A.; Tada, T.; Mizukami, M.; Yagyu, S. *Appl. Phys. Lett.* **2004**, *84*, 130−132.
(29) Yang, X.; Neher, D.; Hertel, D.; Däubler, T. K. *Adv. Mater.* **2004**, *16*, 161−166.
(30) Kim, S. W.; Park, J. H.; Oh, S. S.; Kim, D. Y.; Choi, E. H.; Cho, G. S.; Seo, Y. H.; Kang, S. O.; Park, B.; Saito, Y.; Watanabe, N.; Takezoe, H.; Watanabe, J. *Appl. Phys. Lett.* **2006**, *89*, 213511−213513.
(31) Attar, H. A. A.; Monkman, A. P.; Tavasli, M.; Bettington, S.; Bryce, M. R. *Appl. Phys. Lett.* **2005**, *86*, 121101−121103.
(32) Ding, J.; Zhang, B.; Lü, J.; Xie, Z.; Wang, L.; Jing, X.; Wang, F. *Adv. Mater.* **2009**, *21*, 4983−4986.
(33) Jankus, V.; Monkman, A. P. *Adv. Funct. Mater.* **2011**, *21*, 3350−3356.
(34) Zhang, B.; Tan, G.; Lam, C.-S.; Yao, B.; Ho, C.-L.; Liu, L.; Xie, Z.; Wong, W.-Y.; Ding, J.; Wang, L. *Adv. Mater.* **2012**, *24*, 1873−1877.
(35) Zhen, C.-G.; Dai, Y.-F.; Zeng, W.-J.; Ma, Z.; Chen, Z.-K.; Kieffer, J. *Adv. Funct. Mater.* **2011**, *21*, 699−707.
(36) Earmme, T.; Ahmed, E.; Jenekhe, S. A. *Adv. Mater.* **2010**, *22*, 4744−4748.
(37) Hou, L.; Duan, L.; Qiao, J.; Zhang, D.; Dong, G.; Wang, L.; Qiu, Y. *Org. Electron.* **2010**, *11*, 1344−1350.
(38) Kim, T. H.; Lee, H. K.; Park, O. O.; Chin, B. D.; Lee, S. H.; Kim, J. K. *Adv. Funct. Mater.* **2006**, *16*, 611−617.
(39) Ye, T.; Zhu, M.; Chen, J.; Ma, D.; Yang, C.; Xie, W.; Liu, S. *Org. Electron.* **2011**, *12*, 154−160.
(40) Ge, Z.; Hayakawa, T.; Ando, S.; Ueda, M.; Akiike, T.; Miyamoto, H.; Kajita, T.; Kakimoto, M.-a. *Adv. Funct. Mater.* **2008**, *18*, 584−590.
(41) Jiang, W.; Duan, L.; Qiao, J.; Dong, G.; Zhang, D.; Wang, L.; Qiu, Y. *J. Mater. Chem.* **2011**, *21*, 4918−4926.
(42) Yook, K. S.; Lee, J. Y. *Org. Electron.* **2011**, *12*, 1711−1715.
(43) Yook, K. S.; Lee, J. Y. *Org. Electron.* **2011**, *12*, 1595−1599.
(44) Christian-Pandya, H. K.; Vaidyanathan, S.; Ko, C.; Beyer, F. L.; Galvin, M. E. *Synth. Met.* **2007**, *157*, 120−124.
(45) Yang, C.-C.; Hsu, C.-J.; Chou, P.-T.; Cheng, H. C.; Su, Y. O.; Leung, M.-k. *J. Phys. Chem. B* **2009**, *114*, 756−768.
(46) Schulz, B.; Bruma, M.; Brehmer, L. *Adv. Mater.* **1997**, *9*, 601−613.
(47) Zhang, Y.; Huang, F.; Chi, Y.; Jen, A. K. Y. *Adv. Mater.* **2008**, *20*, 1565−1570.
(48) Adachi, C.; Tsutsui, T.; Saito, S. *Appl. Phys. Lett.* **1989**, *55*, 1489−1491.
(49) Lee, K.; Kim, H.-J.; Cho, J. C.; Kim, J. *Macromolecules* **2007**, *40*, 6457−6463.
(50) Tokuhisa, H.; Era, M.; Tsutsui, T.; Saito, S. *Appl. Phys. Lett.* **1995**, *66*, 3433−3435.
(51) Lian, J.; Liu, Y.; Niu, F.; Zeng, P. *Appl. Surf. Sci.* **2011**, *257*, 4608−4611.
(52) Xiao, L.; Chen, Z.; Qu, B.; Luo, J.; Kong, S.; Gong, Q.; Kido, J. *Adv. Mater.* **2011**, *23*, 926−952.
(53) Ye, T.; Shao, S.; Chen, J.; Wang, L.; Ma, D. *ACS Appl. Mater. Interfaces* **2011**, *3*, 410−416.
(54) Bettenhausen, J.; Strohriegl, P.; Brutting, W.; Tokuhisa, H.; Tsutsui, T. *J. Appl. Phys.* **1997**, *82*, 4957−4961.
(55) Piromreun, P.; Oh, H.; Shen, Y.; Malliaras, G. G.; Scott, J. C.; Brock, P. J. *Appl. Phys. Lett.* **2000**, *77*, 2403−2405.
(56) Jabbour, G. E.; Kawabe, Y.; Shaheen, S. E.; Wang, J. F.; Morrell, M. M.; Kippelen, B.; Peyghambarian, N. *Appl. Phys. Lett.* **1997**, *71*, 1762−1764.
(57) Stossel, M.; Staudigel, J.; Steuber, F.; Blassing, J.; Simmerer, J.; Winnacker, A. *Appl. Phys. Lett.* **2000**, *76*, 115−117.
(58) Jou, J.-H.; Wang, W.-B.; Chen, S.-Z.; Shyue, J.-J.; Hsu, M.-F.; Lin, C.-W.; Shen, S.-M.; Wang, C.-J.; Liu, C.-P.; Chen, C.-T.; Wu, M.-F.; Liu, S.-W. *J. Mater. Chem.* **2010**, *20*, 8411−8416.
(59) Lin, L.; Shia, T. K.; Chiu, C. J. *J. Micromech. Microeng.* **2000**, *10*, 395.
(60) Chen, M.-H.; Chen, Y.-H.; Lin, C.-T.; Lee, G.-R.; Wu, C.-I.; Leem, D.-S.; Kim, J.-J.; Pi, T.-W. *J. Appl. Phys.* **2009**, *105*, 113714−113714.
(61) Wu, C.-I.; Lin, C.-T.; Chen, Y.-H.; Chen, M.-H.; Lu, Y.-J.; Wu, C.-C. *Appl. Phys. Lett.* **2006**, *88*, 152104−152103.
(62) Kohn, W.; Sham, L. J. *Phys. Rev.* **1965**, *140*, A1133−A1138.
(63) Hohenberg, P.; Kohn, W. *Phys. Rev.* **1964**, *136*, B864−B871.
(64) Becke, A. D. *J. Chem. Phys.* **1993**, *98*, 5648−5652.
(65) Hay, P. J.; Wadt, W. R. *J. Chem. Phys.* **1985**, *82*, 299−310.